High brightness electron beam emittance evolution measurements in an rf photoinjector

A. Cianchi,[1,*] D. Alesini,[2] A. Bacci,[3] M. Bellaveglia,[2] R. Boni,[2] M. Boscolo,[2] M. Castellano,[2] L. Catani,[1] E. Chiadroni,[2] S. Cialdi,[3] A. Clozza,[2] L. Cultrera,[2] G. Di Pirro,[2] A. Drago,[2] A. Esposito,[2] M. Ferrario,[2] L. Ficcadenti,[4] D. Filippetto,[2] V. Fusco,[2] A. Gallo,[2] G. Gatti,[2] A. Ghigo,[2] L. Giannessi,[5] C. Ligi,[2] M. Mattioli,[6] M. Migliorati,[2,4] A. Mostacci,[2,4] P. Musumeci,[7] E. Pace,[2] L. Palumbo,[2,4] L. Pellegrino,[2] M. Petrarca,[8] M. Preger,[2] M. Quattromini,[5] R. Ricci,[2] C. Ronsivalle,[5] J. Rosenzweig,[7] A. R. Rossi,[3] C. Sanelli,[2] L. Serafini,[3] M. Serio,[2] F. Sgamma,[2] B. Spataro,[2] F. Tazzioli,[2] S. Tomassini,[2] C. Vaccarezza,[2] M. Vescovi,[2] and C. Vicario[2]

[1]*INFN-Roma "Tor Vergata", Via della Ricerca Scientifica, 1-00133 Rome, Italy*
[2]*INFN-LNF, Via E. Fermi, 40-00044 Frascati, Rome, Italy*
[3]*INFN-Milano, Via Celoria 16, 20133 Milan, Italy*
[4]*Università di Roma "La Sapienza, Dipartimento di Energetica, Via A. Scarpa, 14-00161, Rome, Italy*
[5]*ENEA, Via E. Fermi, 00044 Frascati, Rome, Italy*
[6]*Università di Roma "La Sapienza, Dipartimento di Fisica, Piazzale Aldo Moro 2-00185, Rome, Italy*
[7]*UCLA-Department of Physics and Astronomy, 405 Hilgard Avenue, Los Angeles, California 90095, USA*
[8]*INFN-Roma I, Piazzale Aldo Moro 2, 00185 Roma, Italy*

(Received 24 July 2007; published 4 March 2008)

The new generation of linac injectors driving free electron lasers in the self-amplified stimulated emission (SASE-FEL) regime requires high brightness electron beams to generate radiation in the wavelength range from UV to x rays. The choice of the injector working point and its matching to the linac structure are the key factors to meet this requirement. An emittance compensation scheme presently applied in several photoinjectors worldwide is known as the "Ferrario" working point. In spite of its great importance there was, so far, no direct measurement of the beam parameters, such as emittance, transverse envelope, and energy spread, in the region downstream the rf gun and the solenoid of a photoinjector to validate the effectiveness of this approach. In order to fully characterize the beam dynamics with this scheme, an innovative beam diagnostic device, the emittance meter, consisting of a movable emittance measurement system, has been designed and built. With the emittance meter, measurements of the main beam parameters in both transverse phase spaces can be performed in a wide range of positions downstream the photoinjector. These measurements help in tuning the injector to optimize the working point and provide an important benchmark for the validation of simulation codes. We report the results of these measurements in the SPARC photoinjector and, in particular, the first experimental evidence of the double minimum in the emittance oscillation, which provides the optimized matching to the SPARC linac.

DOI: 10.1103/PhysRevSTAB.11.032801 PACS numbers: 29.27.−a, 41.75.Ht, 07.77.Ka

I. INTRODUCTION

The SPARC [1] project is a research and development photoinjector facility for the generation of high brightness electron beams to drive a SASE-FEL experiment in the visible. The high quality beam produced by SPARC will also allow investigations into the physics of ultrashort beams, plasma-wave based acceleration, and production of x ray by means of Compton backscattering [2]. Moreover, SPARC is the injector prototype for the recently approved SPARX [3] project, a new high brightness electron linac for the generation of SASE-FEL radiation in the wavelength range between 10 and 1 nm to be realized in the Frascati/University of Rome Tor Vergata area. The first phase of the SPARC project is the characterization of the electron beam from the photoinjector at low energy (5.6 MeV with 120 MV/m peak accelerating field on the cathode) before the installation of 3 SLAC-type accelerating sections which boost the beam energy up to 150–200 MeV.

A detailed theoretical study of the emittance compensation process in a photoinjector [4] has demonstrated that its best optimization is achieved by accelerating and propagating the space charge dominated beam through the device following as close as possible two relevant beam equilibrium conditions: the laminar Brillouin flow in drifts and the so-called invariant envelope in accelerating sections, which is a generalization of the Brillouin flow for an accelerated beam. In this regime the beam exhibits emittance oscillations produced by space charge collective forces, called plasma oscillations. Accelerating the beam using the invariant envelope damps these oscillations with the square root of the beam energy. The normalized emittance at the injector output reduces to a steady state minimum when the oscillations are properly tuned. The basic point in the design of a photoinjector is therefore to properly match the beam from the injector into any accelerating section, by means of a laminar waist at injection and a

*Electronic address: alessandro.cianchi@roma2.infn.it

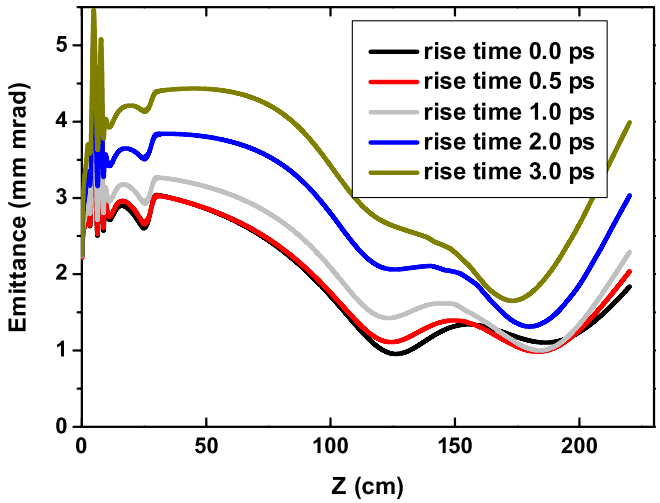

FIG. 1. (Color) Simulation of emittance from the rf gun cathode along the beam line showing the dynamical behavior of the beam for several laser pulse rise times.

transverse match of the invariant envelope to a TW (traveling wave) accelerating field.

Figure 1 shows simulations of the emittance evolution with the typical SPARC parameters for different laser pulse rise times in the drift space downstream the gun. Here and everywhere in this paper, the quoted emittance values are normalized emittances. A flattop distribution with a short rise time leads to a smaller emittance minimum since nonlinear space charge effects are smaller in this configuration. The proper matching to the linac, which in our case starts at 1.5 m from the cathode, requires also careful tuning of the emittance oscillation phase in order to extend the emittance compensation process inside the linac. It has been predicted in Ref. [5] that proper tuning of the emittance oscillation can be achieved by injecting the beam into the linac when the emittance reaches its relative maximum at 1.5 m. In this case, the second emittance minimum will be moved to the linac output. Notice that, if the laser pulse rise time is increased, the optimum matching is found to be on the knee of the emittance oscillation, as also reported in the simulation of [6]. The laminar regime extends up to an energy that for SPARC is around 150 MeV. For this reason, the emittance compensation process of the SPARC injector must be optimized up to the output of the booster linac, before injecting the beam in the undulator through the transfer line.

In order to study the beam dynamics in the rf gun, with particular attention to the above described scenario, a new sophisticated diagnostic tool has been installed and commissioned: the movable emittance meter [7]. With this tool the measurement of the evolution of rms (root mean square) beam sizes, transverse emittances, and transverse phase spaces at different positions along the beam line has been performed and benchmarked with the results of the simulations.

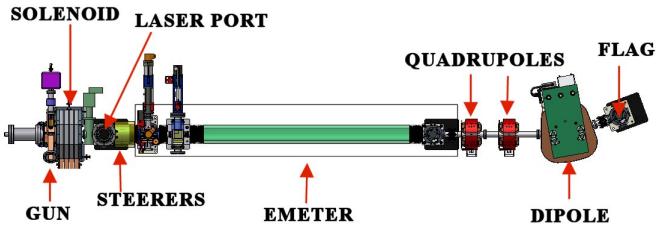

FIG. 2. (Color) Schematic layout of the experiment. Emeter is the abbreviation of the emittance meter.

II. EXPERIMENTAL SETUP

The experimental layout consists of (see Fig. 2): an rf gun, a solenoid, a drive laser beam impinging on a copper cathode at quasinormal incidence reflected by a mirror under vacuum, a couple of steering magnets, the emittance meter, two quadrupoles, a dipole used as a spectrometer, a flag to detect the beam image and measure its energy and the energy spread, and an integrated current monitor (Bergoz model ICT 055-10:1) to measure the current.

During the measurements the typical beam energy was 5.6 MeV, while we have explored different configurations in terms of charge (0.4–1.0 nC), laser energy (50–100 μJ), and laser pulse length (4.0–11.0 ps). The solenoid consists of four separated coils: to obtain a vanishing rotation angle, the coils have been powered in couples with opposite currents. This configuration does not affect the focusing power, which depends on the square of the magnetic field, but simplifies the laser alignment on the cathode because there is a full correspondence between the laser and the electron beam movements. The magnetic field in the solenoid was in the order of 0.3 T. The solenoid cannot be easily moved in any direction.

A. rf gun

The rf gun is one of the most recent generation 1.6 cell S-band BNL/UCLA/SLAC type, a model that overcomes some known deficiencies in the performance of the previous original version [8]. The rf power waveguide is coupled to the full cell, and vacuum is pumped through a symmetrizing port. Two tuners, symmetrically placed in the full cell, are at 90 degrees with respect to the waveguide and the input and output laser ports, half way between the waveguide and the vacuum ports. The symmetry of the structure is important to avoid excitation of dipole components of the electromagnetic field; the lowest perturbation of the rf mode is limited to the quadrupole one, with negligible effects on beam dynamics. The photocathode is centered on the wall of the flange which terminates the half-cell. We use a polycrystal Cu cathode, a material with well tested photoemissive behavior (with a quantum efficiency in typical conditions of about 10^{-4}). The low emission efficiency requires therefore a large laser pulse energy. The cathode needs high vacuum, at the level of 10^{-9} mbar during high gradient operation, so that the pressure without

rf must be 1 order of magnitude lower. In order to fulfill this requirement, the gun is pumped by several pumps: through a direct pumping port, through the waveguide, at the beam port, and behind the cathode plate through an array of small pumping holes. Being the tuner a source of breakdown in some previous guns, a new design and new machining/brazing procedures have been implemented in the construction of the present gun.

B. Laser

The SPARC laser [9], operating in single pulse mode at 10 Hz repetition rate, is a TW-class Ti:sapphire system manufactured by Coherent^{TM}. The laser consists (see Fig. 3) of a Ti:Sa oscillator which generates 100 fs pulses synchronized with the 2856 MHz accelerating field of the linac, within about 1 degree rms (0.973 ps). The oscillator operates at a repetition rate of $791/3$ MHz corresponding to the 36th subharmonics of the rf frequency. It is pumped by the second harmonic of a Nd:YVO4 laser, Verdi by Coherent^{TM}. This laser delivers 5 W CW power at 532 nm. An acousto-optic programmable filter called *DAZZLER* [10] upstream the amplifier is used to control the laser spectrum in order to obtain the desired time profile. The laser amplification process is carried out by a regenerative preamplifier pumped by a 10 W Nd:YLF laser and by two double pass stages excited by the second harmonic of a Nd:YLF with an energy of 0.5 J per pulse. The system delivers pulses at $\lambda = 800$ nm with an energy of about 50 mJ and a repetition rate of 10 Hz. After the amplifier the IR pulses enter a third harmonic generator producing hundreds fs long UV pulses with an energy up to 3 mJ. The frequency up-conversion is required to generate photons with energies larger than the work function of the photocathode. A threshold of 4.59 eV [11] for copper is quoted in the literature. The Schottky effect reduces (at 30 deg from the rf phase zero crossing) the work function in operating conditions to 4.3 eV. Our photon energy is 4.66 eV corresponding to 266.7 nm obtained as the third harmonic of 800 nm. The third harmonic generator consists of two type I beta barium borate (BBO) crystals of 0.5 and 0.3 mm: the harmonic generator produces the second harmonic signal and then the third harmonic one, at $\lambda = 266$ nm, by frequency sum. This stage is followed by an UV stretcher to lengthen the pulse up to 15 ps. An optical transfer line is used to create a beam image on the cathode.

Because of the finite bandwidth of the nonlinear crystals, the slope of the rise and fall times of the resulting flattop pulses cannot be fully controlled by the *DAZZLER*, but after the UV stretcher, due to the large applied chirp, there is a full correspondence between spectral and temporal pulse profiles, opening the possibility of measuring the longitudinal shape of the pulse by simply measuring its spectrum. At this point, if the spectral tails are sharply clipped, it is possible to improve the rise time. To perform this manipulation, we modified the UV stretcher to have a spatial dispersion of the wavelengths. The modified stretcher [12] is a particular version of the $4f$ optical scheme with two gratings and two lenses as shown in Fig. 4.

A collimated beam is sent onto a diffraction grating having 4350 lines/mm at an incidence angle of 43 degrees. The dispersed wavelengths are then focused using a $f = 500$ mm lens located at a distance f from the grating. On the lens focal plane each spectral component reaches the focus in a different spot. On this plane there is full correlation between wavelength and transverse position. This allows any desired amplitude modulation of the spectrum simply by placing a filter or mask at this plane. We used here an iris. The beam is then recollimated by a second lens and sent to another grating which is shifted from the symmetry position by a distance h with respect to a classical $4f$ system. The spectral components are then reflected

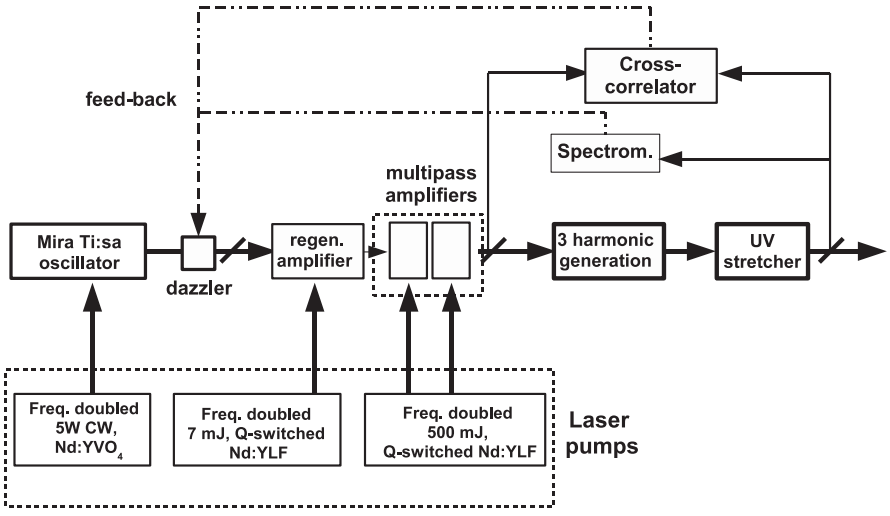

FIG. 3. Schematic layout of the laser system.

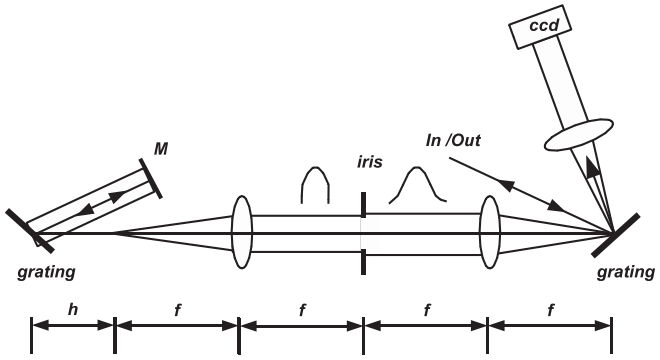

FIG. 4. Layout of the UV stretcher.

by the mirror M and retraced back their path through the system. The shift of the second grating produces an output pulse length proportional to h. In our UV pulse shaping, after the second pass, the fraction of the beam reflected by the grating is focalized by a 30 cm lens onto the plane of a CCD camera. In this way an on-line high-resolution (≈ 0.005 nm) spectrometer is integrated in the shaping system.

C. Emittance meter

The measurements of the beam parameters at different positions z, being z the distance from the photocathode, is fundamental to study the beam dynamics. The emittance meter (see Fig. 5) allows one to follow and completely characterize the transverse phase space evolution along the direction of propagation, for a particular dynamical configuration, i.e., for a given beam density, rf relative phase, and magnetic lens strength.

The beam parameters can be measured in the range from about $z = 1000$ mm to $z = 2100$ mm. The technique [13] of measuring the beam emittance and the phase space in both horizontal and vertical planes makes use of a double system of horizontal and vertical slit masks made of 2 mm thick tungsten. The slit mask must stop, or strongly degrade, the intercepted fractions of the beam. By selecting an array of beamlets by means of an intercepting multislit mask or alternatively by creating one beamlet using a single slit moving transversely over the beam spot, we can divide the space charge dominated incoming beam into emittance-dominated beamlets drifting up to an intercepting screen. Assuming a linear screen response, the intensity of the beamlets spot on the screen is directly proportional to the number of particles in the beamlets hitting the screen. The emittance can be measured estimating the beamlets size [14].

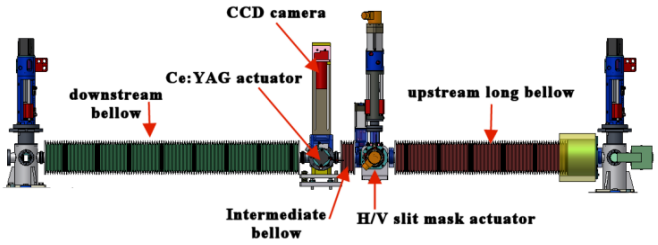

FIG. 5. (Color) A schematic view of the emittance-meter device. Beam direction is from right to left.

Each mask (see Fig. 6) consists of a slit array (7 slits, 50 μm wide spaced by 500 μm, 2 mm thick) and two single slits, 50 and 100 μm wide. The slits are manufactured by electrochemical etching, which provides, in comparison with mechanical machining, higher precision and improved smoothness of the slit edges. Each individual slit was machined as a component of 0.5 mm height and later assembled into the frame [7]. This configuration allows changes of the geometry of the slit mask simply by reshuffling the single components.

The multislit mask was used for single shot measurements, when the beam size was large enough for an adequate beam sampling by the slit array. Alternatively, a single slit was moved across the beam spot in a multishot measurement. In this case the range of transverse sampling can be freely chosen by adjusting the step between the different positions of the slit. Typical values of the sampling distance between the slit positions range from 110 μm to 380 μm. From 9 to 13 beamlets are collected in a single slit scan. No relevant differences were found between single and multislit measurements performed under comparable conditions.

The beamlets emerging from the slit mask are measured by means of a downstream Ce:YAG radiator. The doping level of cerium in the crystal is 0.18%. The response is linear up to 0.01 pC/μm^2 [15], an order of magnitude larger than the maximum density of our beam. Since beam size and divergence depend on the longitudinal position of the device, also the slit to screen distance

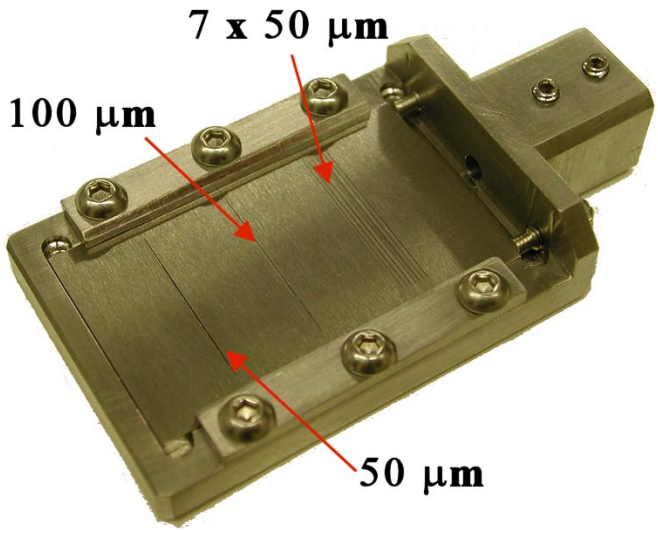

FIG. 6. (Color) Slit mask composed of 7 slits of 50 μm width spaced by 500 μm, one slit of 100 μm width, and one slit of 50 μm width.

must be properly adjusted in order to optimize the beamlets profile measurement. A bellow, placed between the slit mask and the screen, allows one to change their relative distance from 22 to 42 cm, to optimize the drift according to different measurements conditions (converging beam, diverging beam, single, or multislits).

The radiation emitted in the forward direction from the Ce:YAG crystal is collected by a 45 degrees mirror downstream the radiator, on the same screen holder. We observe the back side of the transparent crystal radiator, thus minimizing the degradation of the spatial resolution due of the optics field depth. The small thickness of the crystal (100 μm) prevents appreciable blurring effects due to the crystal bulk emission, as well as significant multiple scattering.

Images are acquired using 8 bit digital CCD cameras (Basler 311 f) equipped with 105 mm ''macro'' type objectives from SIGMA. The chosen magnification of about 0.66 yields a calibration factor near to 15 μm per pixel and a field of view of the screen around 9.6 mm $\times$ 7.2 mm. The angular resolution depends on the drift length between the slits mask and the screen and is in the order of 100 μrad.

The influence on the beam quality of the bellow has been investigated [16]. The bellow has a length of 1.5 m long, and a diameter of 150 mm. Wake field perturbations due to the corrugated structure were studied using the HOMDYN [5] code. The wake fields were computed using the diffractive model of Bane and Sands [17]. This is particularly important when the beam is not well-aligned on-axis. In the case of 1 mm misalignment from the center of the bellow, the contribution of the wakes to the emittance degradation is negligible (0.05%). It remains around 0.13% also at a distance of 4 mm, much larger than the estimated misalignment.

D. Data analysis

Emittance measurements are performed at different z positions. Since the changes in the emittance values are expected to be very small, the measurements must be very accurate. Therefore we developed three different algorithms to process the acquired data. We called MAIN (multiple analysis for image denoising) the algorithm used to obtain the results presented in this paper. It filters the beamlet images and delivers the beam parameters used in the emittance calculation following the method reported in Ref. [14].

The other two, namely, SPEA (single projected ellipse analyzer) and GMESA (genetic multiple ellipse slice analyzer) use the phase space reconstructed from the output of the MAIN algorithm.

We checked the stability of the beam parameters during the time needed for measurements by repeating a number of emittance measurements to control their reproducibility. We obtained results in agreement within the measurement uncertainty.

To minimize the influence of the beam parameters jitter (5% rms for the charge, 2.5% rms for the energy, 150 μm rms for the position of the beam center of mass), we averaged a number of images (from 15 to 30) for each single slit position and projected the intensity distributions onto the horizontal and vertical axes. The profiles filter first selects the region of interest (ROI) of the signal by means of a Gaussian fit. Initial values for mean and maximum amplitude are estimated by smoothing the original profile (with a moving average over 10 pixels), using its maximum as a function amplitude and its position as mean.

To estimate the initial value for the baseline and rms width as required by the fitting procedure, we first define a window, centered around the maximum of the distribution (i.e. the maximum of beamlet profile). The window boundaries define the portion of the distribution that would include the contribution from a beam of 4 mrad maximum divergence, i.e., 4 times the expected value for the beam angular divergence. The baseline is then calculated by averaging the portion of distribution out of the window, while the initial value for the rms width is calculated over the portion of distribution inside it. The fit results are then used to adjust the original profile by subtracting the baseline and limiting the ROI to ± 5 times the rms width around the mean. Noise suppression of the profile curve is obtained by an iterative procedure which computes the rms value, then shrinks the region of interest down to ± 3 times the rms and so on. The procedure stops when the new values match the result of the previous iteration. The algorithm converges typically after 4–5 iterations.

The rms size, the center of mass position and intensity of the beamlets extracted from single image analysis are then cross-checked for fixed z position to ensure that they are self-consistent, and there are no fakes as, for instance, a missing image due to a gun discharge. Data analysis is performed by imposing several thresholds which cut some fraction of the beam. The complete description of the algorithm can be found in Ref. [18].

The results produced by the analysis of the beamlets are samples of the beam phase space. These samples can be used to reconstruct, by interpolation, the phase space of the entire beam (see Fig. 7), the accuracy depending on the number of the collected samples. As an example, the measurements with the single slit mask use 13 beamlets obtained moving the slit transversely for $\pm 3\ \sigma$ (being σ the rms width of the beam distribution) in steps of $\sigma/2$. The resolution in the y' phase-space coordinate is around 100 μrad.

More than just a visual aid in understanding the beam dynamics, the phase space contains important informations. The large signal to noise ratio, given by the high efficiency Ce:YAG crystal (18 000 photons/MeV deposited), allows a detailed reconstruction of the phase space and the calculation of the Twiss parameters.

Starting from the beam phase space, produced by MAIN, the SPEA algorithm calculates the emittance by

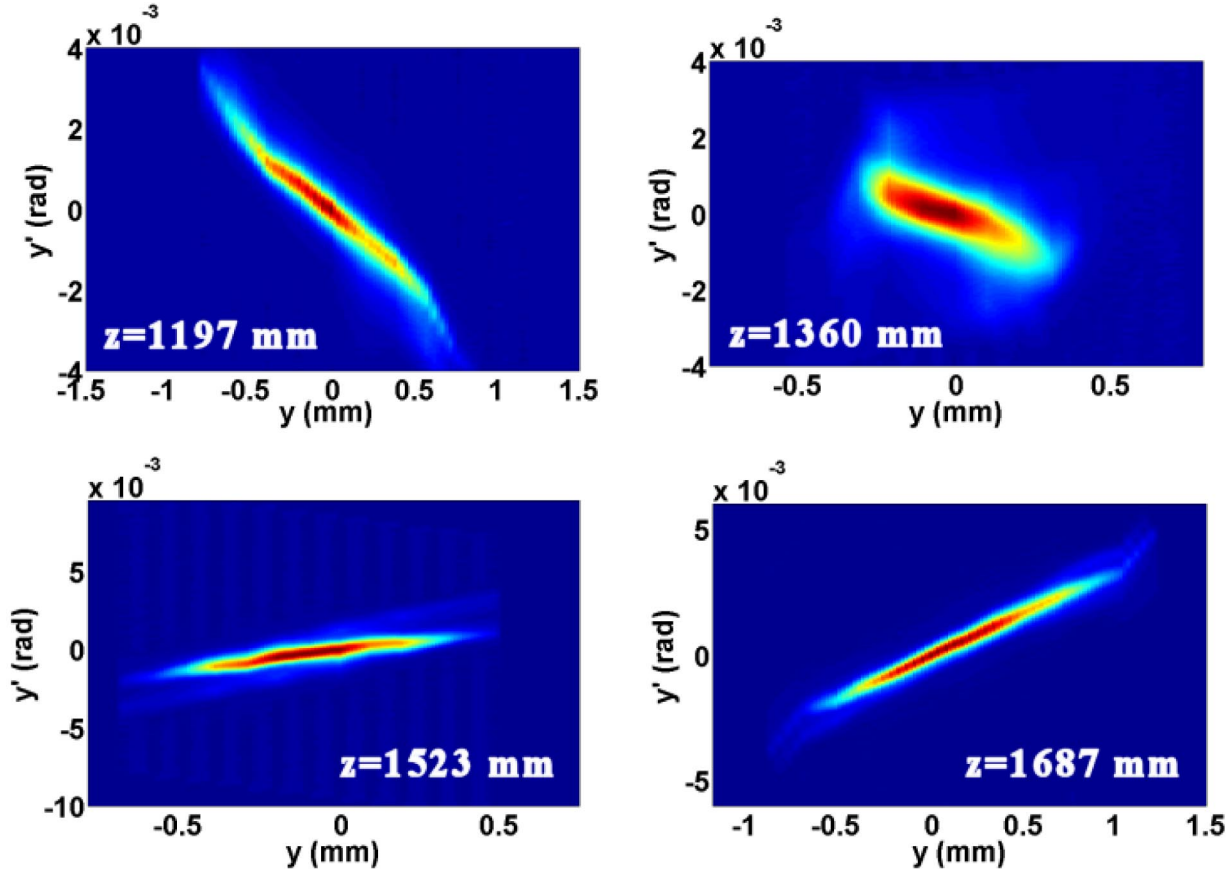

FIG. 7. (Color) Example of phase-space evolution. Data from measurements of run #29 reported later in the paper.

evaluating the second order moment of the distribution. It first defines the region of the phase space belonging to the beam, then starts calculating the second order moment of the distribution on a phase space reconstructed from raw data, by applying background subtraction only. The second order moment are then used to calculated the Twiss parameters.

The beam distribution in phase space is represented by a bitmap image. Each pixel in the bitmap is a 2D bin in the x-x' plane whose value corresponds to the local beam density. From the Courant-Snyder invariant, it is possible to evaluate the contribution of each pixel to the total emittance. All pixels are then sorted by their contribution to the emittance. Iteratively, the pixels giving the highest contribution to the emittance are cut away. In the first iterations they are typically outside the beam core. Then the second order moment and the emittance are calculated again and the pixels sorted again according to their contribution to the emittance.

Also the first and second derivatives of the emittance with respect to the charge (i.e. the integral of the beam distribution in phase space) are calculated, the pixels sorted and cut in a similar way.

It has been shown [19] that the second derivative shows a peak during the iterative process described above. Monte Carlo simulations have demonstrated that this peak appears when the process of removing pixels, initially belonging to background, approaches the beam signal. At this point we can assume that the beam background has been removed and that 100% of the beam charge is selected. If more pixels are cut away, the evaluated emittance decreases. In this way it is possible to define an emittance value as a function of a charge cut.

Comparing emittance values calculated by the MAIN and SPEA algorithms, we find the best agreement for a cut of about 5% resulting in an equivalent emittance of 95% of the beam charge. This allows one to estimate the amount of the charge cut by the MAIN algorithm.

GMESA is based on a genetic algorithm. It starts from the assumption that the projected phase space is the sum of several ellipses somehow related to the longitudinal slices of the beam. The code, using the rules of the genetic algorithms, searches for area and orientation of ellipses that best match the experimental data. More details can be found in Ref. [20].

In Fig. 8 we compare results of the MAIN algorithm against the other two. The MAIN algorithm is used for all results presented in this paper. The good agreement between the algorithms confirms that the MAIN algorithm is well suited for the analysis of our data.

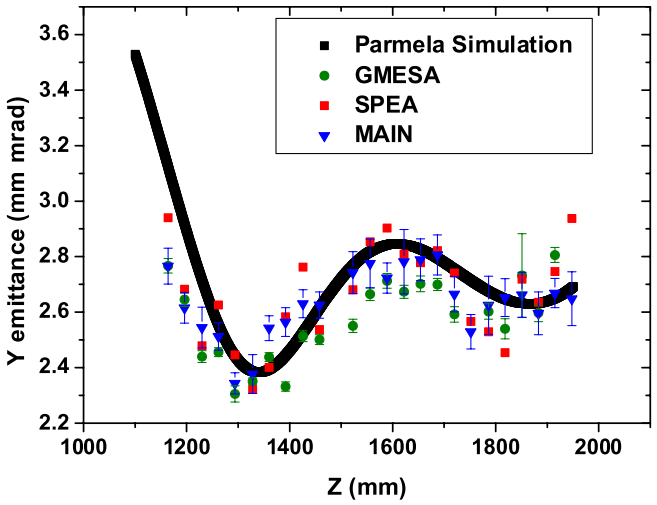

FIG. 8. (Color) Measured vertical emittance along the beam line evaluated by the algorithms MAIN, SPEA, and GMESA compared to a PARMELA simulation. A cut of 5% is applied for SPEA, 3% for GMESA.

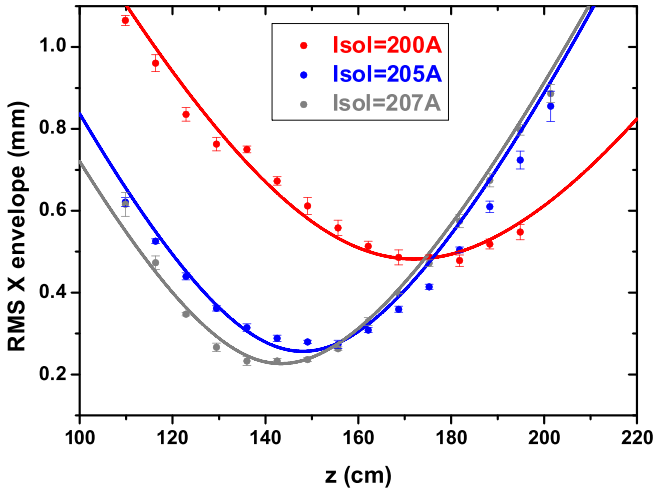

FIG. 9. (Color) An example of rms envelope measurement along the beam line for different solenoid currents. The solid lines are PARMELA simulations.

III. COMPARISON OF MEASUREMENTS WITH SIMULATIONS

A. Comparison strategy

The aim of the comparison between the measurements and the simulations is to verify the coherence of the experimental data with a numerical model describing a beam equivalent to the real one under conditions similar to those of machine operation. The emittance depends on several parameters such as energy, charge, spot size, solenoid focusing field, rf (radio frequency) phase, and laser pulse rise time. The easiest measurement, providing results to compare with simulations, is obtained by moving the emittance meter along the beam line and measuring the horizontal and vertical beam envelopes with the YAG screen (see Fig. 9).

These data are used for the first step of the comparison procedure, which consists in fitting the measured envelope with the two most sensitive parameters, i.e., the laser spot size (measured on the virtual cathode) and the solenoid field strength, while keeping the other parameters constant.

Then a fine adjustment is performed by tuning the other relevant parameters (energy, charge, rf phase) in the range of twice their standard deviations ($\pm$ 5% for the energy, $\pm$10% for the charge, and $\pm$1 degrees for the rf phase). Fifty runs of PARMELA were performed to minimize the difference between the code output and the measurements.

B. Beam model

In the PARMELA [21] model, the temporal profile of the electron beam is assumed to be equal at the cathode to the measured time distribution of the laser pulse (resolution 0.5 ps).

The transverse distribution is described either by a truncated Gaussian or by a stack of uniform disks, depending on which better approximates, run by run, the laser spot image on the virtual cathode. This image is obtained by splitting the laser beam before it enters the vacuum system. As an example, Fig. 10 shows the projected profiles of a measured laser spot for a round beam together with the 2D image of the laser spot. Whenever hot spots are observed, the stack of uniform disks is adopted for a better approximation. The PARMELA SCHEFF 2D routine was used with the parameters shown in Table I, with a radial mesh size automatically adjusted by the code and a variable longitudinal mesh size between 1 and 0.5 cm.

Cross-checks with more time consuming 3D computations (the model is the routine SPCH3D in PARMELA) with Np3 particles have shown equivalent results as the 2D SCHEFF routine corrected for weak ellipticity ($0.9 \leq$ ellipticity ≤ 1.1), which was therefore largely used to speed up calculations.

IV. RESULTS

A. Gaussian pulse

In the early commissioning runs, we started with Gaussian pulses which are the natural output of the laser system. The *DAZZLER* is used to increase the pulse length in order to avoid a transform limited pulse in the output of the amplifier. This was done to prevent damaging the BBO crystal. The UV pulse length on the cathode was controlled by means of the UV stretcher.

Figure 11 shows the longitudinal profile obtained from spectral measurement fitted with a 4.4 ps rms width Gaussian.

Figure 12 shows measurements of the transverse vertical emittance at different z-positions together with a PARMELA simulation.

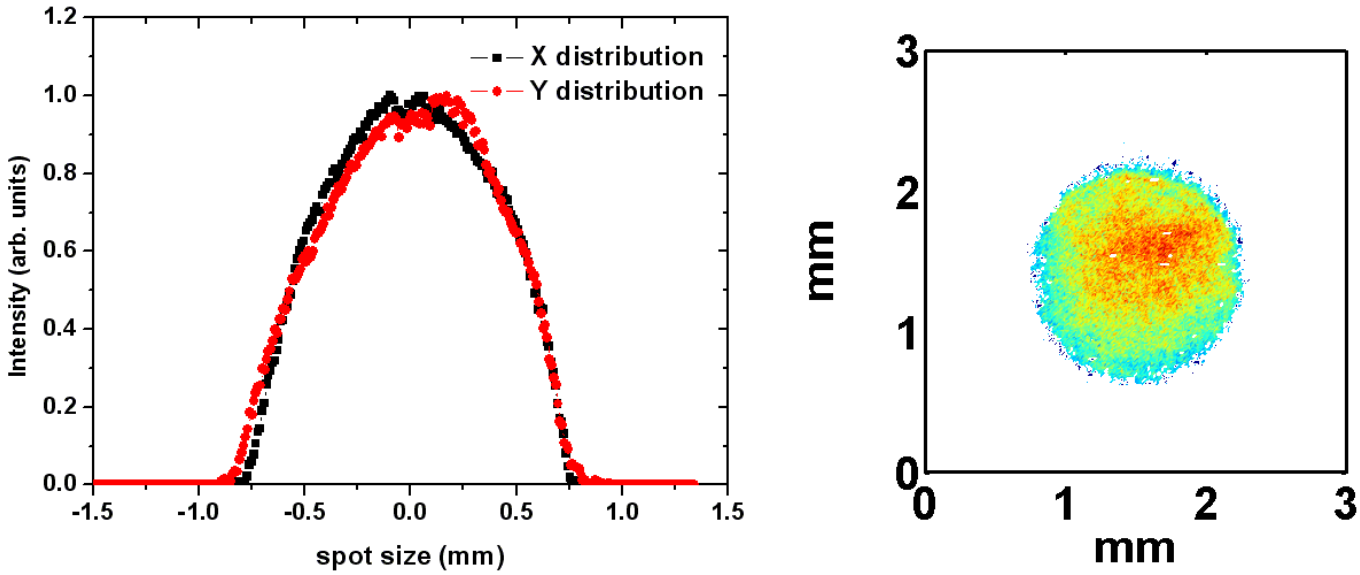

FIG. 10. (Color) Left: Typical projected transverse profile of the laser spot on the virtual cathode. Right: 2D laser spot profile.

TABLE I. Parameters used in PARMELA simulation.

Parameter	Description
Nr = 20	Number of radial meshes
Nz = 200	Number of longitudinal meshes
Np = 2×10^4	Number of particles
Np3 = 10^5	Number of particles for 3D routine

The error bars are calculated in the following way. Because of the multishot feature of our measurement, the primary source of uncertainty are beam fluctuations. To measure an emittance value at given longitudinal position, we need a set of profiles, one at each transverse slit position. All images taken at a given transverse slit position are equivalent. Then every image can be grouped with the others coming from different transverse slit positions to obtain a complete set of profiles to measure the emittance value. In this way a number N of such independent sets can be obtained. The emittances computed by each of those sets are equivalent and independent. Therefore, the result of the emittance measurement $\overline{\epsilon}$ can be computed as the average and the measurement uncertainty $u(\epsilon)$ as the standard deviation of the average (according to Type A evaluation of uncertainty [22]). The choice of N is user dependent; our strategy is to take the maximum number of meaningful emittances. The length of the error bars is the expanded uncertainty with a confidence level of 95%; the expanded uncertainty is obtained by multiplying the

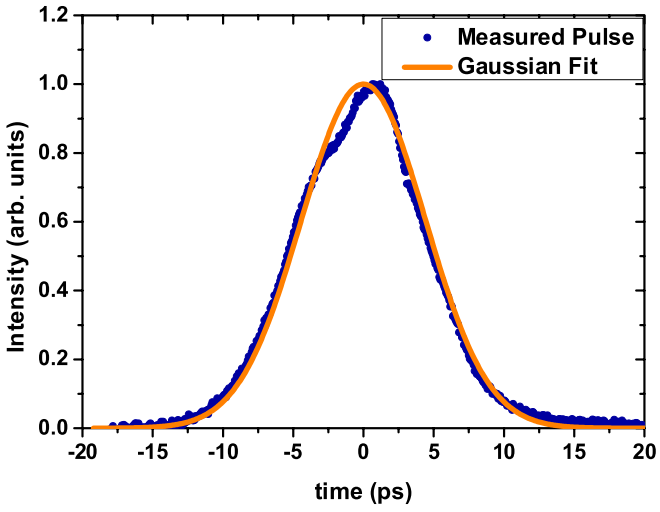

FIG. 11. (Color) Longitudinal shape for a Gaussian-like laser pulse obtained from a spectral measurement as described in Sec. II A compared with an ideal Gaussian.

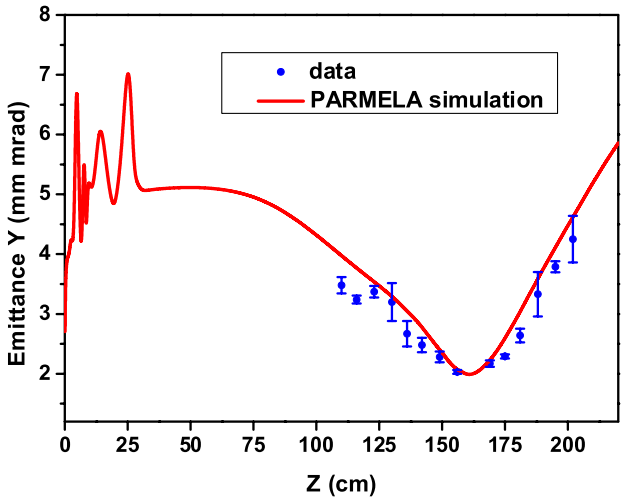

FIG. 12. (Color) Emittance measurement using the longitudinal laser pulse shape of Fig. 11. A PARMELA simulation is also shown for comparison.

TABLE II. Parameters of the beam corresponding to the emittance measurement shown in Fig. 12.

Parameter	Value
Energy	5.65 MeV
Charge	1 nC
Laser spot size	450 μm
Laser pulse length	10 ps FWHM
Phase ($\varphi - \varphi_{\max}$)	5^0

standard uncertainty $u(\epsilon)$ for a coverage factor depending on the confidence level and the degrees of freedom of the measurement (i.e. N in our case), according to Ref. [22]. Concerning the systematic errors, the main one is the energy measurement. Since this error is only a scale factor and does not influence the relative dependence of the emittance on the longitudinal position, we did not include it in the plots. We estimate that, in the worst case, it is smaller than 4%. The relevant parameters are shown in Table II.

The phase $\varphi_{\max}$ is the rf phase corresponding to the maximum energy measured in the spectrometer. The value 5 deg means that there is a difference of 5 degrees with respect to the phase where the energy is maximum in the direction of the minimum energy spread. Figure 13 shows the values of the energy and the energy spread versus phase to clarify this point. The error bars represent the standard deviation of the values averaged over 50 pulses. The absolute value of the phase is meaningless. We look for the maximum of the energy and we move in the direction of the minimum energy spread, in this case towards positive values of the phase. The energy spread is the overall correlated energy spread.

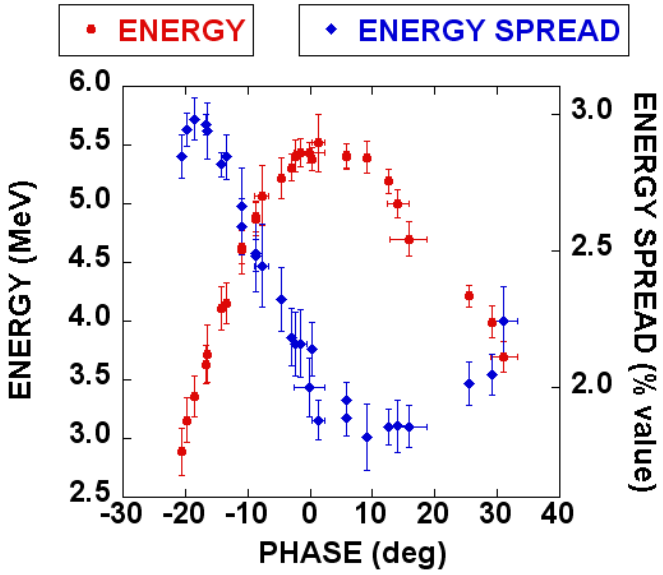

FIG. 13. (Color) Energy and energy spread versus phase. The measurement is the result of averaging 30 pulses.

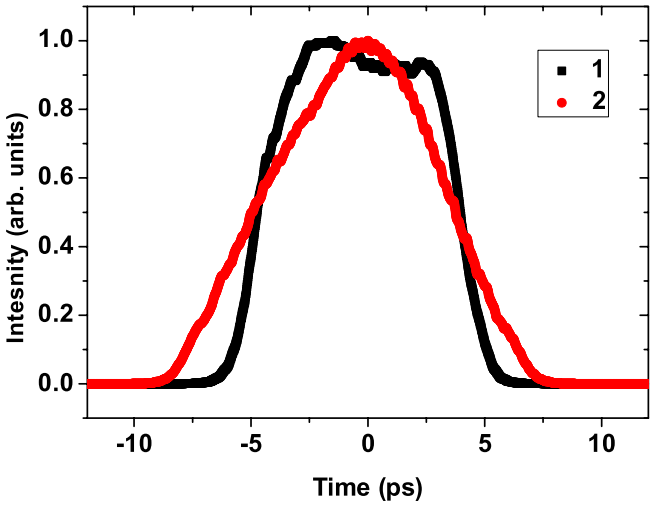

FIG. 14. (Color) Two different pulse shapes with the same FWHM = 8.7 ps: (1) rise time ≈ 2.5 ps; (2) rise time ≈ 5 ps.

B. Laser pulse shape studies

Studies were performed in order to check the dependence of the beam parameters on rf phase and laser parameters, mainly the pulse shape and pulse length, with particular attention to the laser pulse rise time, defined as the time needed for the pulse intensity to grow from 10% to 90% of the maximum one.

In the following, we show the comparison between results obtained with two different longitudinal laser pulses. Figure 14 shows the time profiles calculated from spectral measurements as described in Sec. II B.

The parameters are reported in Table III. The rise time was about 2.5 ps for spectrum 1 and about 5 ps for spectrum 2 of Fig. 14. The corresponding emittance evolution in the vertical plane is shown in Fig. 15.

The beam dynamics is different in the two cases because it is strongly dependent on the laser rise time. The minimum emittance value is about 25% smaller in the case of shorter rise time, confirming the result of Ref. [23].

C. High brightness beam

A large number of emittance-meter scans have been done in the drift region after the gun to maximize the

TABLE III. Parameters of the two beams corresponding to the emittance measurement shown in Fig. 15.

Parameter	Value
Energy	5.4 MeV
Charge	0.74 nC
Laser spot size	310 μm
Laser pulse length	8.7 ps FWHM
Phase ($\varphi - \varphi_{\max}$)	8^0
Rise time beam 1	2.5 ps FWHM
Rise time beam 2	5.0 ps FWHM

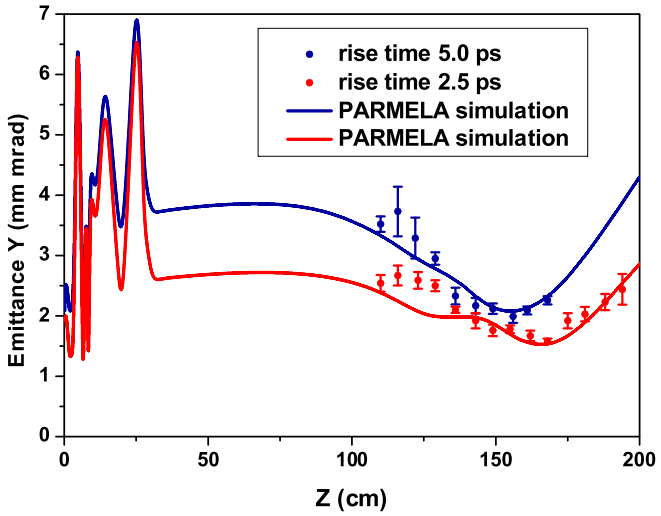

FIG. 15. (Color) Vertical emittance evolution for the beams with the longitudinal profiles of Fig. 14 and parameters of Table III.

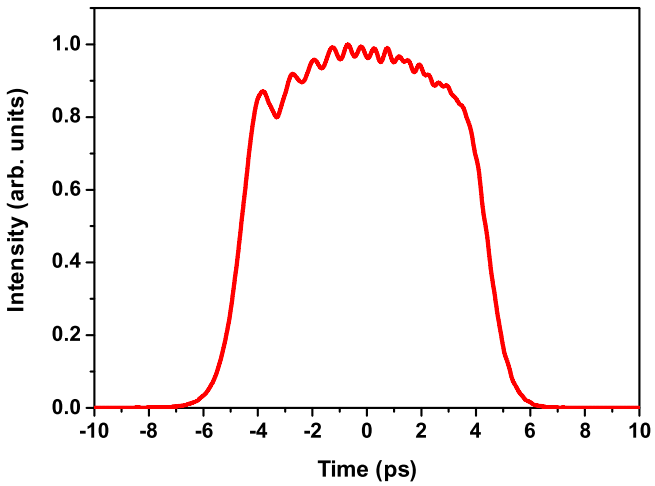

FIG. 17. (Color) Longitudinal laser profile. The pulse length is 9 ps FWHM, and the rise time is about 2.7 ps. The best brightness has been obtained with this profile.

brightness, defined as $B = 2I/\epsilon_x\epsilon_y$, with I representing the peak current and $\epsilon_{x,y}$ the transverse emittances. The optimization parameters were the injection phase, the solenoid strength, the longitudinal profile of the laser, and the transverse beam spot size. The design goal was 2 mm mrad for the transverse emittance, 100 A for the beam current, and thus 5×10^{13} A/m^2 for the brightness. The plots in Fig. 16 summarize the results of the measurements showing, in a sample of several runs with a brightness larger than the design value, the peak brightness normalized to its design value and the normalized emittance.

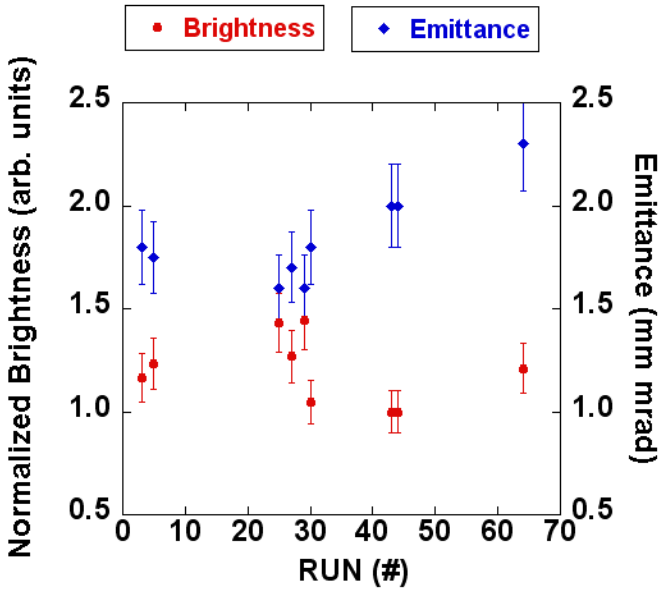

FIG. 16. (Color) Vertical emittance and brightness normalized to their design values, in the cases with peak brightness larger than its design value (5×10^{13} A/m^2).

In order to find the brightness values, we used the laser bunch length measured at the cathode to calculate the beam current and the minimum emittance value measured in the drift. Therefore we neglected the bunch length increase due to the space charge longitudinal defocusing along the drift. Simulations show that, in the measurements conditions, the bunch lengthening is less than 10%, which is within the uncertainty of the charge measurement. We also performed some electron pulse length measurements with an Hamamatsu streak camera (model C1370) using an aerogel as radiator. The time resolution of this streak camera is not better than 1 ps. We could not distinguish between the lengths of the electron bunch and of the laser pulse.

The best brightness has been obtained with the longitudinal profile shown in Fig. 17; the beam parameters are given in Table IV. The results in Fig. 18 show the measured emittance evolution versus z for a beam of 92 A peak current.

The minimum emittance value is 1.65 ± 0.06 mm mrad, yielding a peak brightness of $7.0 \pm 0.8 \times 10^{13}$ A/m^2. The injection phase was set to -8.0 ± 0.5 deg with respect to the maximum energy gain phase and the laser rms spot size was 360 μm. The solid line in the plot is a simulation made with PARMELA as discussed in Sec. III.

TABLE IV. Parameters of the beam corresponding to the best brightness result.

Parameter	Value
Energy	5.65 MeV
Charge	0.83 nC
Laser spot size	360 μm
Laser pulse length	8.9 ps FWHM
Phase ($\varphi - \varphi_{\max}$)	8^0

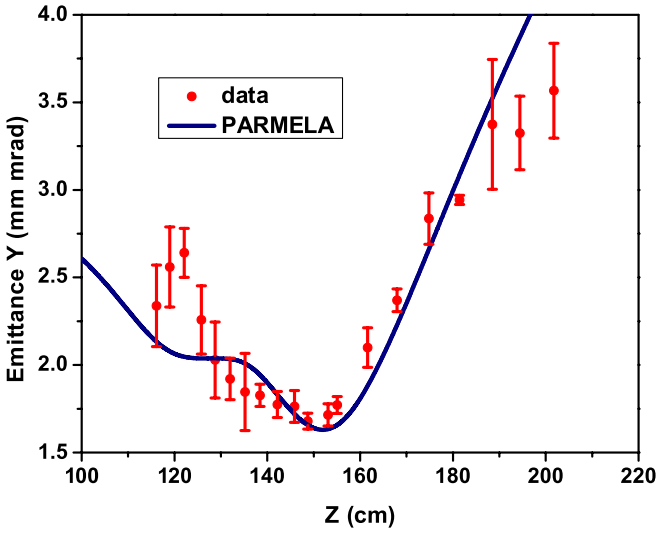

FIG. 18. (Color) Vertical emittance versus z for run #29. This is the measurement with the highest brightness of about 7×10^{13} A/mm^2. A PARMELA simulation is also shown.

D. Double minimum oscillation

The emittance oscillation observed in the simulation of a photoinjector is an important feature of the Ferrario working point [5]. Some of the photoinjectors running worldwide or in the design stage, like for instance FERMI [24], PAL [25], LCLS [5], BESSY FEL [26], XFEL [6] are based on this working point. The optimized matching with the SPARC linac relies on this peculiar space charge regime which works in the flattop pulse mode and guarantees the optimum matching to the invariant envelope in the linac sections, yielding therefore the minimum emittance at the linac output. Emittance oscillations of this kind have been explained as the effect of a beating between head and tail plasma frequencies caused by correlated chromatic effects in the solenoid [27]. We have obtained a direct evidence of this type of oscillation working with short laser rise time ($\cong$ 1.5 ps, the longitudinal profile is shown in Fig. 19). To enhance this effect, we move the injection phase above the maximum energy gain phase, thus inducing a higher energy spread ($\approx$ 3%), although the minimum achievable emittance in this case is slightly worse. The parameters of such a beam are given in Table V.

The result of this measurement, showing double minimum oscillation of the emittance is shown in Fig. 20. It is worth remarking that this is the first direct measurement of double minimum oscillation in a photoinjector ever done.

The effect of this oscillation can also be observed in the transverse phase space. In this dynamic regime, the head and tail of the bunch experience a different focusing when passing through the solenoid, due to the space charge correlated energy spread which is strongly enhanced at the bunch ends. As a consequence, at the z position of the relative emittance maximum a cross shape structure in the transverse phase space is predicted by simulations with a flattop longitudinal distribution of the laser pulse (see Fig. 21 on the right). Under laminar conditions, i.e., when the solenoid field is not so high to cause crossover, the space charge dominated waist is reached at different positions by the head and the tail slices of the bunch, so that

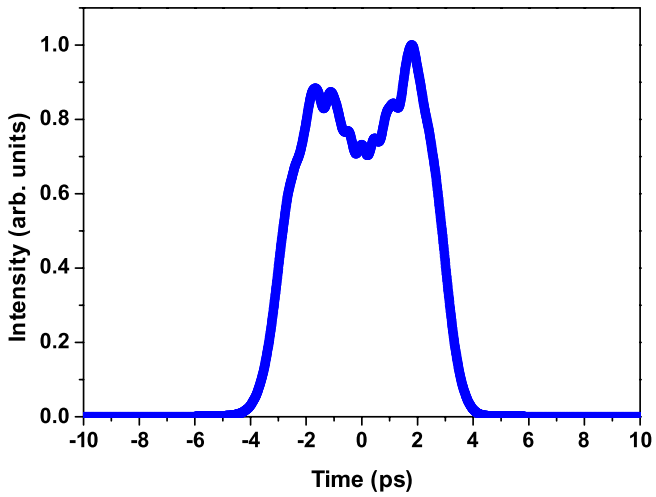

FIG. 19. (Color) Longitudinal profile of the laser for the measurement shown in Fig. 20. The rise time is 1.5 ps and the FWHM is 5.5 ps.

TABLE V. Parameters of the beam whose emittance measurement is shown in Fig. 20.

Parameter	Value
Energy	5.5 MeV
Charge	0.5 nC
Laser spot size	450 μm
Laser pulse length	5.5 ps FWHM
Phase ($\varphi - \varphi_{max}$)	12^0

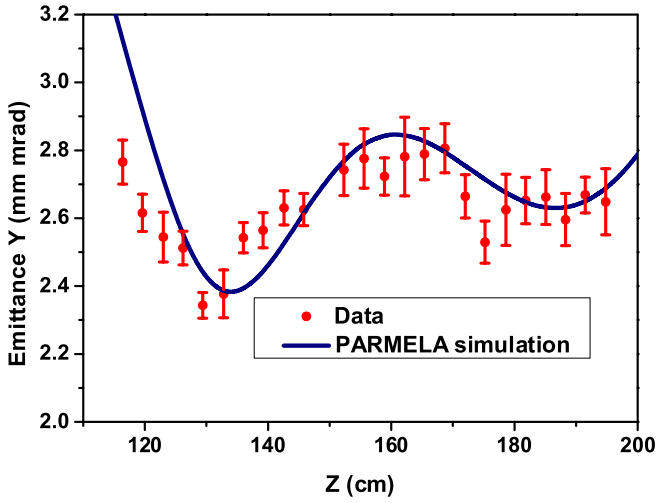

FIG. 20. (Color) Vertical emittance measurement showing a double minimum oscillation. A PARMELA simulation is also shown on the same plot for comparison.

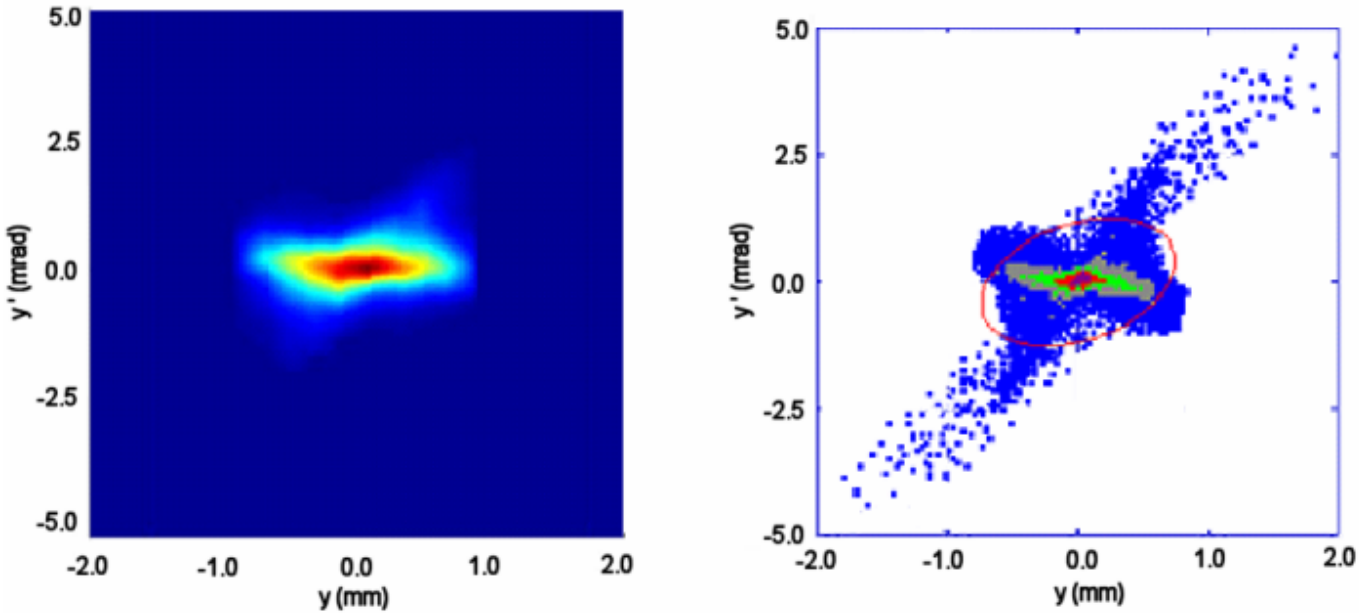

FIG. 21. (Color) On the left: measured transverse phase space in the vertical plane at $z = 1500$ mm from the cathode. On the right: PARMELA simulation obtained with the parameters of the measurement.

when the bunch tail is already diverging the bunch head is still converging.

We have measured this effect and the comparison between PARMELA simulation and measured phase space is shown in Fig. 21. Even if it is hard to compare them quantitatively, the measured phase space exhibits this particular cross shape structure as predicted by simulation.

V. CONCLUSIONS

The beam of the SPARC photoinjector has been studied and characterized with a completely new diagnostic device called emittance meter, which yields a measurement of the beam envelope and emittance at different distances from the cathode, providing information on the transverse phase spaces as well.

The emittance meter actually defines a new kind of beam envelope diagnostics since it measures the evolution of the beam dynamics.

Improvements in the laser settings and changes in either the solenoid field or alignment, just to mention the most relevant, can be easily and quickly checked using fast automatic procedures. The possibility of having several measurements along the beam line gives a better understanding of the dynamics and a more direct comparison with the simulations.

The obtained results are of particular relevance. Innovative techniques for laser pulse time shaping have been developed to create a flattop profile with fast rise time.

After realizing a high brightness electron beam, larger than its design value of 5×10^{13} A/m^2, we have compared several laser beam shapes by measuring the emittance and reconstructing the dynamics, using also the information coming from the transverse phase space.

The comparison between simulations and experimental results has been presented as well.

The experimental evidence of the double minima in the emittance oscillation, predicted by simulations and observed for the first time in the SPARC photoinjector, is of particular interest. It provides a direct validation of the theory on which the Ferrario working point [5] is based. This result has been confirmed by the analysis of the reconstructed phase space where a clear signature of this dynamical scenario has been identified.

ACKNOWLEDGMENTS

The authors wish to thank all SPARC collaboration scientists and engineers who contributed to the design and commissioning of the emittance meter. Special thanks to V. Lollo for his contribution to the mechanical design, engineering, and bench testing of the system, F. Anelli and S. Fioravanti for their work on motor controllers. Also thanks to A. Battisti, L. Antonio Rossi, and S. Stabioli. This work has been partially supported by the EU Commission in the sixth framework program, Contract No. 011935 EUROFEL-DS1, and from the MIUR-Progetti Strategici DD1834.

[1] D. Alesini *et al.*, Nucl. Instrum. Methods Phys. Res., Sect. A **507**, 345 (2003).

[2] D. Alesini *et al.*, in Proceedings of EPAC 2006, Edinburgh, Scotland, p. 2439.

[3] C. Vaccarezza, in Proceeding of 37th ICFA Advanced Beam Dynamics Workshop on Future Light Sources, Hamburg, Germany, 2006, p. 30.
[4] L. Serafini and J. B. Rosenzweig, Phys. Rev. E **55**, 7565 (1997).
[5] M. Ferrario, J. E. Clendenin, D. T. Palmer, J. B. Rosenzweig, and L. Serafini, SLAC-PUB 8400.
[6] M. Ferrario, K. Flöttmann, T. Limberg, P. Piot, and B. Grigoryan, TESLA FEL 2001-03.
[7] L. Catani *et al.*, Rev. Sci. Instrum. **77**, 093301 (2006).
[8] J. B. Rosenzweig, A. M. Cook, M. P. Dunning, P. Frigola, G. Travish, C. Sanelli, and F. Tazzioli, in Proceedings of PAC 2005, Knoxville, TN, USA (2005).
[9] S. Cialdi, M. Petrarca, and C. Vicario, Opt. Lett. **31**, 2885 (2006).
[10] F. Verluise, V. Laude, J. P. Huignard, P. Tournois, and A. Migus, J. Opt. Soc. Am. B **17**, 138 (2000).
[11] S. Graves, L. DiMauro, R. Heese, E. Johnson, J. Rose, J. Rudati, T. Shaftan, and B. Sheehyi, in Proceedings of PAC 2001, Chicago, USA (2001), p. 2439.
[12] S. Cialdi, C. Vicario, M. Petrarca, and P. Musumeci, Appl. Opt. **46**, 4959 (2007).
[13] B. E. Carlsten, J. C. Goldstein, P. G. O'Shea, and E. J. Pitcher, Nucl. Instrum. Methods Phys. Res., Sect. A **331**, 791 (1993).
[14] C. Lejeune and J. Aubert, Adv. Electron. Electron Phys. Suppl. A **13**, 159 (1980).
[15] D. Filippetto, Ph.D. thesis, University of Rome La Sapienza, 2007 (to be published at http://padis.uniroma1.it/).
[16] A. Cianchi *et al.*, in Proceedings of EPAC 2004, Lucerne, Switzerland (2004), p. 2622.
[17] K. Bane and M. Sands, SLAC-Pub-4441.
[18] D. Filippetto, Sparc Note SPARC/EBD-07/002.
[19] A. Cianchi, C. Ronsivalle, L. Giannessi, M. Quattromini, M. Castellano, and D. Filippetto, Sparc Note SPARC/EBD-07/003.
[20] A. Bacci, Sparc Note SPARC/EBD-07/004.
[21] L. M. Young, Los Alamos National Laboratory Report No. LA-UR-96-1835.
[22] *International Organization for Standardization, Guide to Expression of Uncertainty in Measurement* (ISO, Geneva, 1995).
[23] J. Yang, F. Sakai, T. Yanagida, M. Yorozu, Y. Okada, K. Takasago, A. Endo, A. Yada, and M. Washio, J. Appl. Phys. **92**, 1608 (2002).
[24] Carlo Bocchetta *et al.* (Fermi Collaboration), *FERMI@Elettra Conceptual Design Report* (Sincrotrone, Trieste, 2007), http://www.elettra.trieste.it/docs/FERMIelettra-CDR.pdf.
[25] S. J. Park, J. H. Park, Y. W. Parc, C. B. Kim, C. D. Park, J. S. Oh, J. Y. Huang, I. S. Ko, D. Xiang, and X. Wang, in *Proceedings of FEL 2005, Stanford, California, USA* (2005), p. 600.
[26] F. Marhauser, in Proceedings of EPAC 2004, Lucerne, Switzerland (2004).
[27] M. Ferrario, M. Boscolo, V. Fusco, C. Vaccarezza, C. Ronsivalle, J. B. Rosenzweig, and L. Serafini, *The Physics and Application of High Brightness Electron Beam* (World Scientific, Singapore, 2002).